

Mutual Inductance Calculation of Rectangular Coils With Convex Torus Finite Magnetic Shields in Wireless Power Transfer

Zhongqi LI, Qian ZHANG, Lingjun KONG, Changxuan HU, and Shoudao HUANG

Abstract—Mutual inductance is one of the critical parameters of wireless power transfer systems, and the accurate calculation of mutual inductance is considered an essential theoretical basis for designing and optimizing wireless power transfer systems. However, the problem of calculating the mutual inductance of a bilateral bounded magnetically shielded rectangular coil with a convex toroid still needs to be solved. Therefore, this article proposes a spatial boundary separation analysis method and derives vector magnetic potential expressions for each region with convex toroidal magnetic shielding structure using the double Fourier transform and Maxwell's equations. The mutual inductance calculation formula under the spatial position are obtained using boundary conditions and spatial geometric relationships. In contrast to traditional approximation methods, the mutual inductance calculation method of this article permits an accurate numerical solution for the mutual inductance between rectangular coils. The 4.69% difference between calculated and experimental mutual inductance values confirms the accuracy of the computational method in this research. The proposed model of this article matches the transmission efficiency of the conventional rectangular disc coil at over 97% for the same specifications and reduces material usage by 11.12%.

Index Terms—Magnetic shielding, radio energy transmission, reciprocal inductance calculation, rectangular coils.

I. INTRODUCTION

WIRELESS power transfer (WPT) technology is a non-contact power transmission technology [1]–[2] that is

gradually surpassing traditional power transmission methods in terms of safety, reliability. Hence, WPT technology holds considerable promise for evolutionary progress in the domain of engineering applications and has been successfully applied to electric vehicles [3]–[4], portable electronics [5]–[6], biomedical science [7]–[8], and power supply for underwater environments [9]–[10], etc., and is now becoming an increasing research focus in the field of electrical engineering. In designing and optimizing the structure of a WPT system, the mutual inductance (MI) is a core variable affected by the transmission performance, and the efficient and accurate calculation of the MI is a crucial component of this process. The structural design of the WPT system shows corresponding differentiation due to the diversity of application scenarios, with different system structures producing different MI coefficients, which in turn have varying degrees of influence on the system transmission efficiency. Therefore, it is of great importance to research methods for accurately calculating the coupling coefficients of MI models.

The coil acts as a crucial element in WPT systems. With the wide application of WPT technology, various types of coils have emerged, including rectangular, circular, polygonal, cross-shaped, and so on. The current coil designs commonly include two primary forms, rectangular and circular. However, from a practical point of view, rectangular coil structures are more necessary and practical in specific application scenarios for WPT systems. This is because lower MI variations are exhibited by rectangular coils compared to circular coils when the coils are shifted relative to each other, which provides more excellent resistance to shifting and results in more stable transmission efficiency. Among them, MI calculation methods in circular coil structures have been the subject of many studies. In contrast, MI calculation methods for rectangular coil structures have been studied less frequently. The work on rectangular coil structures is based on Maxwell's equations, Biot-Savart law [11]–[12], Bessel's function [13]–[14], and Fourier series [15].

In a related study for MI modeling without the addition of magnetic shielding materials, [16] proposes a novel analytical calculation method. This method treats a multi-turn coil as multiple single-turn coils and MI calculation when the coils are vertically offset. Yet, it is not possible to realize MI calculation methodology when the coils in this mod-

Manuscript received December 24, 2024; revised February 28, 2025; accepted March 17, 2025. Date of publication June 30, 2025; date of current version April 18, 2025. This work was supported in part by Natural Science Foundation of Hunan Province under the grant 2022JJ30226, National Key R&D Program Project under the grant 2022YFB3403200, Key Projects of Hunan Provincial Department of Education under the grant 23A0432, Excellent Youth Project of Scientific Research of Hunan Provincial Department of Education under the grant 22B0577, National Natural Science Foundation of China (NSFC) Youth Science Fund Project under the grant 62303178, and Scientific Research Fund of Hunan Provincial Education Department under the grant 23C0182. (Corresponding author: Zhongqi Li.)

Z. Li, Q. Zhang, L. Kong, and C. Hu are with the College of Traffic Engineering, Hunan University of Technology, Zhuzhou 412007, China (email: my3eee@126.com; 3489734@qq.com; 2119551072@qq.com; 905436194@qq.com).

S. Huang is with the College of Electrical and Information Engineering, Hunan University, Changsha 410082, China (e-mail: hsd1962@hnu.edu.cn).

Digital Object Identifier 10.24295/CPSS TPEA.2025.00015

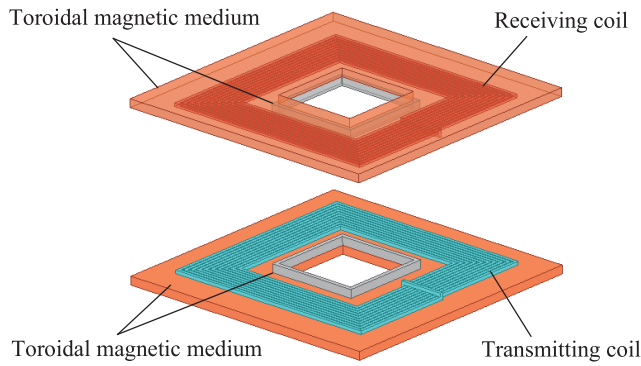


Fig. 1 Three-dimensional view of a rectangular coil of bounded magnetic medium with a convex toroidal type.

el are horizontally misaligned. [17] proposes to construct an MI model using the vertex method to achieve coupling coefficient calculation of rectangular coils of arbitrary dimensions when horizontally offset. Although the MI at the horizontal offset of the coil is calculated by the vertex approach, the MI has not been studied when coils are angularly deflected. In [18], by multiplying the helix factor k , it was realized to determine the MI of a rectangular helical coil at vertical and horizontal offsets as well as at angular deflections. An abstract approach is adopted in [19] by considering wires as ideal line segments of infinitesimal cross-section and calculating the MI between two any positioned quadrilateral coils by accumulating the MI of two straight wires at any position.

In the practical application of WPT systems, magnetic shielding materials are usually integrated the MI model. The addition of magnetic shielding can effectively diminish the risk of magnetic radiation, and it changes the magnetic flux path and enhances the inter-coil coupling effect. An analytical model based on Bessel-Fourier transform and dyadic Fourier transform is proposed in [20] to calculate MI for horizontal offsets between the coils with ferrite added on the transmitting coil side, while disregarding the width-thickness ratio. In [21], the MI at any position between rectangular coils with magnetic media on the side of the transmitting coil only and a bounded thickness of the magnetic media is calculated using Fourier integration and spatial transformation methods. However, the length of the magnetic medium is not considered, while in practical applications, the size of the magnetic medium is limited. [22] presents the solution for the calculation of MI between rectangular coils with a bounded magnetic shielding on the side of the transmitting coils at arbitrary positions, which is based on hyperbolic functions and Fourier series expansions, in contrast to [21] where the boundaries of the magnetic medium are considered. [23] uses the separated variable method in order to calculate the MI of a rectangular coil with both side magnetic shielding. While the dimensions of the magnetic shielding are considered, it is not possible to realize the calculation of MI of a structure with bounded magnetic shielding and rectangular coils. The MI model has been proposed in [24] by means of a subdomain division based method in order to calculate the MI at an arbitrary location

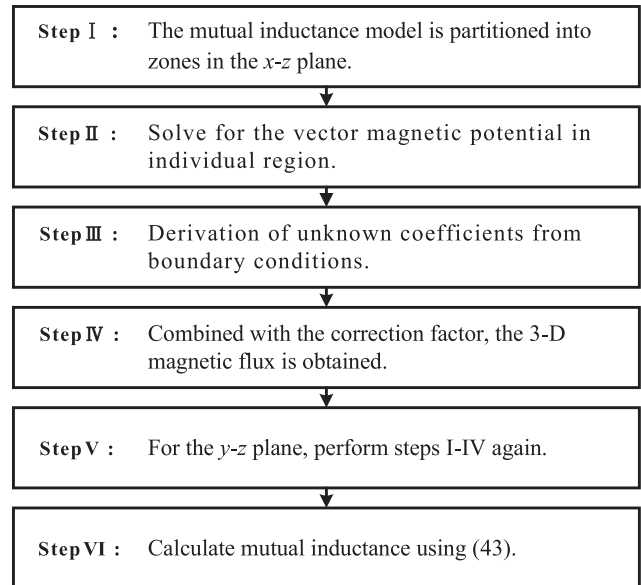


Fig. 2 MI calculation flowchart.

between rectangular coils with bounded magnetic shielding. Although the model provides an accurate solution for systems with bilateral bounded magnetic shielding materials, the conservation of magnetic shielding materials has not yet been fully considered. Therefore, the skeletonization of the magnetic shielding material can be considered, but it is inevitable that skeletonization will diminish the performance of the magnetic shielding material. [25] verified the shielding performance of ring-type magnetic shielding material, and it was found that the shielding performance of ring-type magnetic shielding material is similar to that of rectangular disk magnetic shielding material under the same specifications.

In brief, the challenge of calculating the MI of bilateral bounded magnetically shielded rectangular coils with a convex toroidal shape is still unsolved. In view of the above, a computational model for the MI of the bilateral bounded magnetically shielded rectangular coil with a convex toroid has been established in this article, as depicted in Fig. 1.

The computation of MI a rectangular coil with convex toroidal bilateral bounded magnetic shielding is realized using the spatial boundary separation analysis method in this article. In the end, the feasibility and accuracy of putting forward computational methodology are validated through simulation and experiment. Under the exact specifications, the MI can reach over 97% of that of the rectangular disk magnetic shielding transmission structure while saving up to 11.12% of the magnetic shielding material.

II. ANALYTICAL TWO-DIMENSIONAL MODEL FOR A RECTANGULAR COIL WITH CONVEX TOROIDAL MAGNETIC SHIELDING

The MI calculation process is divided into six steps, as illustrated in Fig. 2. Initially, the MI model is segmented into multiple sectors along the horizontal and vertical directions. Second-

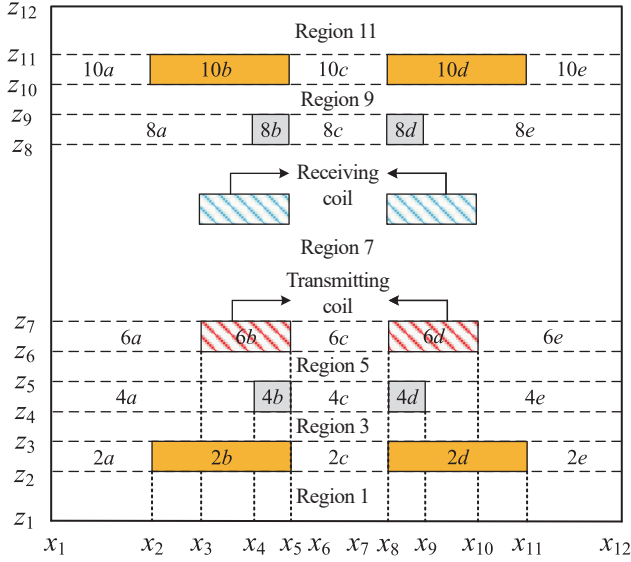


Fig. 3 Cross-sectional view of the x - z plane for a rectangular coil with a convex torus magnetic shielding.

ly, the vector magnetic potential flux equations of each region are obtained through Poisson and Laplace equations. Then, the unknown coefficients in the vector magnetic potential flux equations are determined by applying boundary conditions, and the correction factors are utilized to correct B-field of the two-dimensional model. The same steps are applied to the y - z section. Ultimately, magnetic flux density in the 3D model is achieved through superposition calculation, and subsequently, the MI is determined using formula. The detailed steps for the MI calculation are illustrated in Fig. 2.

A. 2D Model Analysis

In order to attain a magnetic shielding performance comparable to that of the rectangular disk magnetic shielding material and to optimize the transmission structure model, adding another layer of magnetic shielding material above the magnetic shielding region of the MI model, thereby constructing a rectangular planar coil structure with a convex-type ring-type magnetic shielding, as depicted in Fig. 3. The system is initially segmented into different sectors according to material properties. Subsequently, the vector magnetic potential were derived for the individual regions. In the end, this includes the solution of unknown coefficients, the coupling of equations, and the transformation of a matrix.

Fig. 1 shows a three-dimensional illustration of the system under consideration. The rectangular coils in the figure are referred to as transmitting and receiving coils or primary and secondary coils, respectively. A zigzag ring-type magnetic shielding material surrounds the dielectric above and below. In the WPT system, the transmitting coil is located above the magnetically shielded region on the transmitting side and the receiving coil is located below the magnetically shielded region on the receiving side. This system uses two rectangular coils with the same geometry and magnetic shielding material. The

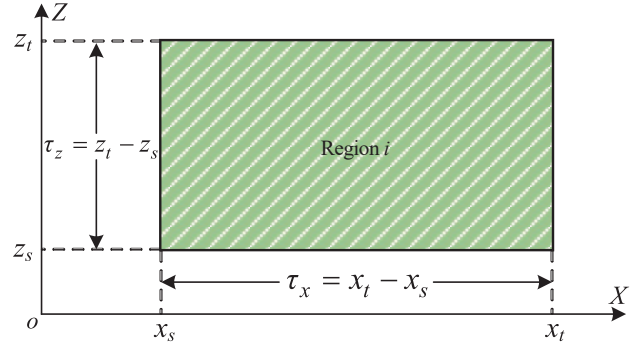


Fig. 4 Cartesian coordinate representation of region i .

proposed model is applicable for coils and magnetic shielding of different sizes.

A detailed x - z plane cross-section of the system, used to formulate the 2D subdomain model, is illustrated in Fig. 3. The entire system is divided horizontally and vertically into zones based on the nature of the different media and the structure of the system. Region 1 is designated as the air medium below the magnetic shielding material, and region 11 is designated as the air medium above the magnetic shielding material. Regions 2 and 4 and regions 8 and 10 are represented by a cabochon-type magnetic shielding material, typically linear, isotropic, and homogeneous. Regions 2a, 4a, 8a, and 10a are located on the left side of the magnetically shielded area and regions 2e, 4e, 8e, and 10e are located on the right side of the magnetically shielded area. To save on consumables, the system is hollowed out for the magnetic media, with regions 2c, 4c, 8c, and 10c representing the air areas resulting from the hollowing out of the magnetic media. Region 5 denotes an air region, located immediately below the transmitting coil region. Region 7 represents an air region, located immediately above the transmitting coil region. Because the transmitting coil does not carry current, it is not divided into subregions in region 7. Regions 3 and 9 are represented by acceptable air gaps in the middle of the convex ring-type magnetic media. Regions 6a and 6e denote air regions, immediately adjacent to the transmitting coil in region 6. Regions 6b and 6d denote current source regions, located above the magnetic shielding region on the transmit side. The region 6b is oriented in the same direction as the third direction y , and the region 6d is oriented in the opposite direction to the third direction y . Region 6c represents the air region and is located in the middle of the transmitting coil regions 6b and 6d.

Region i , as defined in Fig. 4, can correspond to any region ranging from region 1 to region 11. The boundaries and scope of the area are defined in the diagram.

The initial and terminal coordinates of region i are denoted by x_s and x_t in the x -direction, and by z_s and z_t in the z -direction, respectively. The specific value of x_s , x_t , z_s , and z_t in the i -region can be derived in Fig. 3. For instance, if $i=6b$, this indicates that the values of x_s , x_t , z_s , and z_t in region 6b are x_3 , x_5 , z_6 , and z_7 .

The magnetic flux density of the target region can be solved for only if the magnetic vector potential of the target region is calculated, and the vector magnetic potential of each region is

derived from (1) and (2). The exact derivation process is presented in the next section.

B. Vector Magnetic Potential Derivation

The stimulation current I_p passes along the transmitting coil, which, under the action of I_p , produces a varying magnetic field. The reason is that the receiving coil exists within the impact of the magnetic field of the transmitting coil. So it achieves electromagnetic coupling and produces a current under the influence of the varying H-field.

To facilitate the computation of the H-field, the magnetic vector potential of the Lorentz norm is introduced. Magnetic vector potential (MVP) is a vector field in classical electromagnetism used to describe magnetic flux density. Magnetic flux density (MFD) is a underlying attribute of H-field, used to depict the distribution of H-field in spatial extent.

In the presence of a current density region, the MVP is controlled by the Poisson equation, as indicated by (1).

$$\frac{\partial^2 A_r}{\partial x^2} + \frac{\partial^2 A_r}{\partial z^2} = 0 \quad (1)$$

where J denotes the current density. In other regions with no current density, the MVP is controlled by the Laplace equation, as given by (2).

$$\frac{\partial^2 A_r}{\partial x^2} + \frac{\partial^2 A_r}{\partial z^2} = -\mu_0 J \quad (2)$$

The MVP is determined by deriving (1) and (2) through the method of separation of variables. Then MFD is further calculated.

$$B_r = \nabla \times A_r \quad (3)$$

where A_r represents MVP in the r region. Calculating MFD allows further calculation of H-field.

$$H_r = B_r / \mu_r \mu_0 \quad (4)$$

Both μ_r and μ_0 denote the relative magnetic permeability. μ_r denotes the medium in the r region, and μ_0 denotes the air medium.

The generalized formula for MVP in the region $6b$ and $6d$ is obtained by deriving (1). The components of MVP in the MI model are represented by (5). The other regional vector magnetic potential expressions are obtained by solving (2) and are given in (6).

$$A_r = (A_r^x + A_r^z + A_r^s) \vec{e}_r \quad (5)$$

$$A_r = (A_r^x + A_r^z) \vec{e}_y \quad (6)$$

where the y -component of the r -region magnetic vector potential, considering only the $z = z_s$ and $z = z_t$ boundary conditions is denoted by A_y^x ; similarly, A_y^z represents the y -part of the r -region MVP considering only the $x = x_s$ and $x = x_t$ boundary conditions. A_y^s denotes the vector magnetic potential under

the current source area, which exists only in region $6b$ and $6d$. The expressions for the MVP in each region, derived from the solutions of Poisson's or Laplace's equations, will be provided below.

1) Regions 2b, 2d, 4b, 4d, 6b, 6d, 8b, 8d, 10b, 10d

The MVP in these regions is derived from (1), with the expressions for A_y^x , A_y^z , and A_y^s being given by (7), (8), and (9), respectively.

$$A_y^x = (z_t - z) \cdot c_0 + (z - z_s) \cdot d_0 + \sum_{N_r=1}^{N_r} \cos \left[a_{N_r}^r (x - x_s) \right] \cdot \left\{ \frac{c_r^x \sinh \left[\alpha_{N_r}^r (z_t - z) \right]}{\alpha_{N_r}^r \sinh \left(\alpha_{N_r}^r \tau_z \right)} + \frac{d_r^x \sinh \left[\alpha_{N_r}^r (z - z_s) \right]}{\alpha_{N_r}^r \sinh \left(\alpha_{N_r}^r \tau_z \right)} \right\} \quad (7)$$

$$A_y^z = \sum_{L_r=1}^{L_r} \sin \left[\beta_{L_r}^r (z - z_s) \right] \cdot \left\{ \frac{f_r^z \cosh \left[\beta_{L_r}^r (x_t - x) \right]}{\beta_{L_r}^r \sinh \left(\beta_{L_r}^r \tau_x \right)} + \frac{e_r^z \cosh \left[\beta_{L_r}^r (x - x_s) \right]}{\beta_{L_r}^r \sinh \left(\beta_{L_r}^r \tau_x \right)} \right\} \quad (8)$$

$$A_y^s = -0.5 \mu_0 J \cdot z^2 \quad (9)$$

where a particular region is denoted by r , N_r and L_r denote the number of harmonics in this MI model, where N_r denotes the harmonic parameter in the horizontal direction and L_r denotes the harmonic parameter in the vertical direction. And c_0 , d_0 , c_r^x , d_r^x , e_r^x , and f_r^x denote unknown coefficients. $\alpha_{N_r}^r$ and $\beta_{L_r}^r$ denote the spatial frequencies in this MI model. $\alpha_{N_r}^r$ and $\beta_{L_r}^r$ are given by (10).

$$\alpha_{N_r}^r = N_r \pi / \tau_x, \quad \beta_{L_r}^r = L_r \pi / \tau_z \quad (10)$$

2) Regions 3, 5, 7, 9

In regions 3, 5, 7, and 9, the medium may not be air; however, it is assumed to have zero electrical conductivity and a magnetic permeability of μ_0 . The magnetic vector potential is also zero when $x = x_s$ or x_t . Consequently, the Laplace equation is applied, and (11) provides the vector magnetic potential expression for A_y^z in these regions.

$$A_y^z = \sum_{N_r=1}^{N_r} \sin \left[\alpha_{N_r}^r (x - x_s) \right] \cdot \left\{ -\frac{c_r^z \cosh \left[\alpha_{N_r}^r (z_t - z) \right]}{\alpha_{N_r}^r \sinh \left(\alpha_{N_r}^r \tau_z \right)} + \frac{d_r^z \cosh \left[\alpha_{N_r}^r (z - z_s) \right]}{\alpha_{N_r}^r \sinh \left(\alpha_{N_r}^r \tau_z \right)} \right\} \quad (11)$$

3) Regions 1, 11

In regions 1 and 11, the range of calculations for the magnetic field is limited. Hence, the MVP is assumed to be 0 under conditions $z = z_1$, $z = z_{12}$, $x = x_1$, and $x = x_{12}$. The vector magnetic potential expression for regions 1 and 11 of $A_y^z = 0$ is given by (12), following applying Laplace's equation.

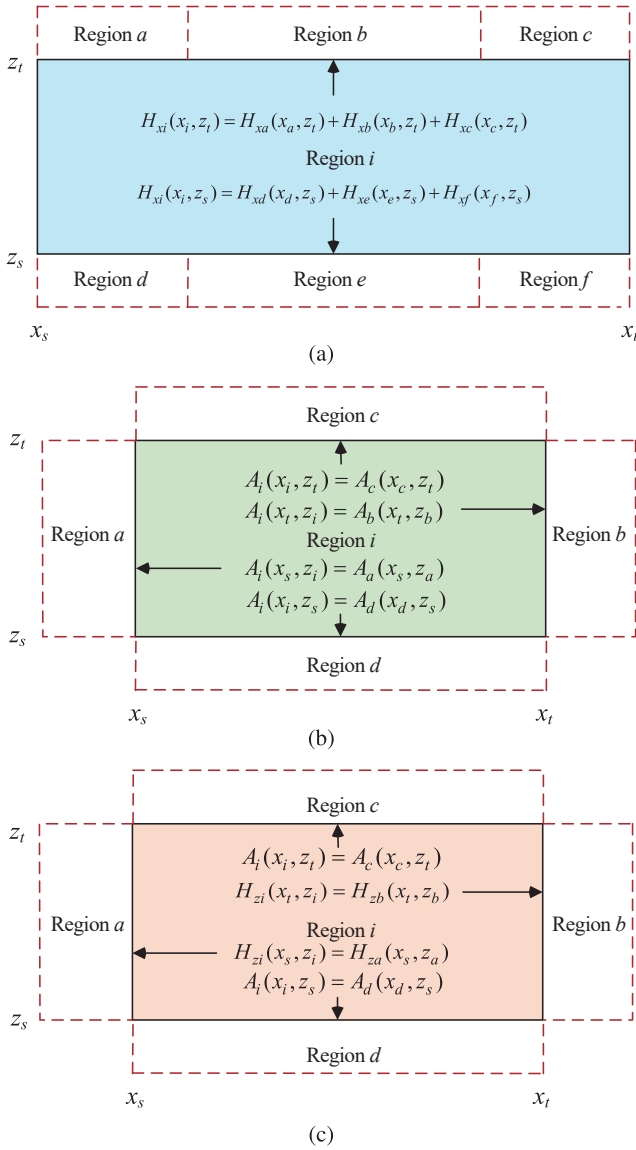


Fig. 5 Boundary condition model (a), (b) and (c).

$$A_y^x = \sum_{n=1}^N \sin \left[\alpha_n^r (x-x_s) \right] \cdot \left\{ -\frac{c_r^x \sinh \left[\alpha_n^r (z_t-z) \right]}{\alpha_n^r \cosh \left(\alpha_n^r \tau_z \right)} + \frac{d_r^x \sinh \left[\alpha_n^r (z-z_s) \right]}{\alpha_n^r \cosh \left(\alpha_n^r \tau_z \right)} \right\} \quad (12)$$

4) Regions 2c, 4c, 6c, 8c, 10c

The medium in all regions is air, indicating that the Laplace equation governs the MFD in these regions. In the derivation process, by applying the critical values of MVP and MFD on the boundaries of these regions as boundary conditions, the generalized form of MVP for these regions can be derived.

$$A_y^x = \sum_{n=1}^N \sin \left[\alpha_n^r (x-x_s) \right] \cdot \left\{ \frac{c_r^x \sinh \left[\alpha_n^r (z_t-z) \right]}{\alpha_n^r \sinh \left(\alpha_n^r \tau_z \right)} + \frac{d_r^x \sinh \left[\alpha_n^r (z-z_s) \right]}{\alpha_n^r \sinh \left(\alpha_n^r \tau_z \right)} \right\} \quad (13)$$

$$A_y^z = \sum_{l=1}^{L_i} \sin \left[\beta_l^r (z-z_s) \right] \cdot \left\{ \frac{e_r^z \sinh \left[\beta_l^r (x_t-x) \right]}{\beta_l^r \sinh \left(\beta_l^r \tau_x \right)} + \frac{f_r^z \sinh \left[\beta_l^r (x-x_s) \right]}{\beta_l^r \sinh \left(\beta_l^r \tau_x \right)} \right\} \quad (14)$$

5) Regions 2a, 2e, 4a, 4e, 6a, 6e, 8a, 8e, 10a, 10e

The magnetic field in all regions, being an air medium, is controlled by the Laplace equation. The y -part of the MVP in the r -region, A_y^x , is considered concerning only the z -side boundary conditions, and the y -part of the MVP in the r -region, A_y^z , is considered concerning only the x -side boundary conditions. Fig. 3 illustrates that the MVP is zero on the x -edge in x_{pr} regions 2a, 4a, 6a, 8a, and 10a, and zero on the x -edge x_{qr} in regions 2e, 4e, 6e, 8e, and 10e. Thus, $e_r^z = 0$ is substituted into (14) to obtain the magnetic vector potentials in regions 2a, 4a, 6a, 8a, and 10a. The same can be obtained; however, for regions 2e, 4e, 6e, 8e, and 10e, $f_r^z = 0$ is substituted into (14) to obtain the magnetic vector potential.

C. Calculation of Unknown Coefficients

As illustrated in Fig. 5, the offered 2D subdomain analysis model showcases three distinct boundary condition patterns. In regions 1, 3, 5, 7, 9, and 11, the boundary condition illustrated in Fig. 5 is to be used. Since more than one region is connected to the z -edge of region r , the boundary conditions $F(x)$ and $G(x)$ on the z -edge are represented as segmented mapping. For region 1, x_{pr} applied at the lower boundary is zero, while for region 11, x_{qr} applied at the upper boundary is zero.

The pattern of boundary conditions in Fig. 5 must be applied in regions 2a, 2c, 4a, 4c, 6a, 6c, 8a, 8c, 10a, 10c, 2e, 4e, 6e, 8e, and 10e. The A_y^z on the left boundary x_s is zero in regions 2a, 4a, 6a, 8a, and 10a, and the A_y^z on the correct boundary x_t is also zero in regions 2e, 4e, 6e, 8e, and 10e, according to the special boundary relationship between regions. The boundary condition illustrated in Fig. 5 is to be used in regions 2b, 2d, 4b, 4d, 6b, 6d, 8b, 8d, 10b, and 10d.

After determining the boundary conditions between the 11 partitions and 31 subregions of the MI model, the coefficients to be determined for individual regions are calculated by the system of coupled equations. The subsequent part is dedicated to the derivation of the unknown coefficients within the vector magnetic potential. To elucidate the derivation progression, one of the neighboring side of region 6b is utilized as a case study.

In accordance with (7), The following expression for $A_{y_{6b}}^x$ on the edge of the bottom $z = z_6$ of region 6b can be obtained.

$$A_{y_{6b}}^x \Big|_{z=z_6} = \tau_{z_6} \cdot c_{0_{6b}} + \sum_{n_{6b}=1}^{N_{6b}} \frac{c_{6b}^x}{\alpha_{n_{6b}}} \cdot \cos \left[\alpha_{n_{6b}}^{6b} (x-x_3) \right] + A_{y_{6b}}^s \Big|_{z=z_6} \quad (15)$$

The relationship between $A_{y_{6b}}^x$ and $A_{y_5}^x$ is obtained by applying the MVP as a boundary condition on $z = z_6$, ensuring the continuity of the MVP between the regions.

$$A_{y_3} \Big|_{z=z_0} - A_{y_6}^s \Big|_{z=z_0} = \tau_{z_1} \cdot c_{0_6} + \sum_{n_{6s}=1}^{N_{6b}} \frac{c_{6b}^x}{\alpha_{n_{6b}}} \cdot \cos \left[\alpha_{n_{6b}}^{6b} (x-x_3) \right] \quad (16)$$

In the above equation, the series in the equation is viewed as the Fourier Series (FS) containing just the cosine factor. On the interval $[x_3, x_4]$, the FS expansion of $L(x) = A_{y_3} \Big|_{z=z_0} - A_{y_6}^s \Big|_{z=z_0}$ is performed to determine the coefficients c_{0_6} and c_{6b}^x .

$$c_{0_6} = \frac{1}{\tau_{x_{11}}} \cdot \frac{1}{\tau_{z_{11}}} \cdot \int_{x_3}^{x_4} L(x) dx \quad (17)$$

$$c_{6b}^x = \frac{2}{\tau_{x_{11}}} \int_{x_3}^{x_4} \alpha_{n_{6b}}^{6b} \cdot L(x) \cdot \cos \left[\alpha_{n_{6b}}^{6b} (x-x_3) \right] dx \quad (18)$$

After the expression for $A_{y_3} \Big|_{z=z_0}$ has been substituted into c_{0_6} and c_{6b}^x (17) and (18) can be rewritten as (19) and (20), where $n_{6b}=1,2,3 \dots N_{6b}$.

$$c_{0_6} + \sum_{n_5=1}^{N_5} [c_{\omega}^x \cdot Tc(n_5) + d_{6\omega}^x \cdot Td(n_5)] = e \quad (19)$$

$$c_{\omega}^x + \sum_{n_5=1}^{N_5} [c_{\omega}^x \cdot Tc(n_{6b}, n_5) + d_{6\omega}^x \cdot Td(n_{6b}, n_5)] = 0 \quad (20)$$

In (19), $Tc(n_5)$ and $Td(n_5)$ are related only to n_5 . The variable s is related to the current source.

$$Tc(n_5) = \frac{\text{csch}(\alpha_{n_5}^5 \cdot \tau_{z_5})}{\tau_{x_{6\omega}} \cdot \tau_{z_{6\omega}} \cdot \alpha_{n_5}^5} \int_{x_3}^{x_4} \sin \left[\alpha_{n_5}^5 (x-x_1) \right] dx \quad (21)$$

$$Td(n_5) = \frac{-\text{coth}(\alpha_{n_5}^5 \cdot \tau_{z_5})}{\tau_{x_{6\omega}} \cdot \tau_{z_{6\omega}} \cdot \alpha_{n_5}^5} \int_{x_3}^{x_4} \sin \left[\alpha_{n_5}^5 (x-x_1) \right] dx \quad (22)$$

$$e = - \frac{A_y^s \Big|_{z=z_0}}{\tau_{z_6}} = \frac{0.5\mu_0 \cdot \mu_{6b} \cdot J_y \cdot z_6^2}{\tau_{z_6}} \quad (23)$$

In (20), $Tc(n_{6b}, n_5)$ and $Td(n_{6b}, n_5)$ are determined by n_{6b} and n_5 .

$$Tc(n_{6b}, n_5) = \frac{2\alpha_{n_{6b}}^{6b} \cdot \text{csc}(\alpha_{n_5}^5 \cdot \tau_{z_5})}{\tau_{x_{6\omega}} \cdot \alpha_{n_5}^5} \cdot \int_{x_3}^{x_4} \sin \left[\alpha_{n_5}^5 (x-x_1) \right] \cdot \cos \left[\alpha_{n_{6b}}^{6b} (x-x_3) \right] dx \quad (24)$$

$$Td(n_{6b}, n_5) = - \frac{2\alpha_{n_{6b}}^{6b} \cdot \text{coth}(\alpha_{n_5}^5 \cdot \tau_{z_5})}{\tau_{x_{6\omega}} \cdot \alpha_{n_5}^5} \cdot \int_{x_3}^{x_4} \sin \left[\alpha_{n_5}^5 (x-x_1) \right] \cdot \cos \left[\alpha_{n_{6b}}^{6b} (x-x_3) \right] dx \quad (25)$$

Matrix representations are more readable, concise, and ex-

pandable than systems of equations, thus the coefficients to be determined for regions 5 and 6b are defined by the matrix, this matrix is a column vector of $(2N_5 + 1 + N_{6b}) * 1$. The current source matrix is a column vector of $(1 + N_{6b}) * 1$.

$$[D_{5\&6b}] = [c_1^x \ c_5^x \ d_1^x \ d_5^x \ c_{0_6}^x \ c_{6b}^x]^T \quad (26)$$

$$[O_{5\&6b}] = \left[- \frac{A_y^s \Big|_{z=z_0}}{\tau_{z_6}} \ 0 \ 0 \right]^T \quad (27)$$

According to the array of equations, the length of the matrices of c_{0_6} and c_{6b}^x in region 6b is $(1 + N_{6b} * 1)$. The above system of equations can be expressed by (28).

$$[K_{5\&6b}] [D_{5\&6b}] = [O_{5\&6b}] \quad (28)$$

In the above equation, $[K_{5\&6b}]$ is the system information matrix that is associated with regions 5 and 6b, which encompasses the dimensions, relative permeability, and conductivity of the two-dimensional subdomain model.

$$[K_{5\&6b}] = [[T_{5\&6b}] [I_{5\&6b}]] \quad (29)$$

where $[T_{5\&6b}]$ is the matrix of $(1 + N_{6b}) * 2N_5$ and $[I_{5\&6b}]$ is the unit matrix that is of $(1 + N_{6b}) * (1 + N_{6b})$.

The complete form of (28) can be obtained by determining the coefficients by repeating the above method, utilizing other boundary conditions in each region, as demonstrated in (30).

$$[K] [D] = [O] \quad (30)$$

$[D]$ is a column vector of length $L_{\max} * 1$, including all undetermined coefficients in the entire region.

$$[D] = [[D_1]^T [D_2]^T \dots [D_{31}]^T]^T \quad (31)$$

$[D_r]$ is the matrix of coefficients to be determined for a region in a two-dimensional subdomain, and L_{\max} is the sum of the number of coefficients to be determined in the subdomain, L_{\max} is denoted by (32).

$$L_{\max} = N_1 + 2N_2 + L_2 + \dots + 2(N_{4b} + 1 + L_{4b}) + \dots + N_{31} \quad (32)$$

$[K]$ represents the $L_{\max} * L_{\max}$ system information matrix, and $[O]$ is the electromagnetic source matrix of length $L_{\max} * 1$. The coefficients to be determined can ultimately be calculated using (33).

$$[D] = [K]^{-1} [O] \quad (33)$$

III. MUTUAL INDUCTANCE CALCULATION FOR RECTANGULAR COILS ENCLOSED BY CONVEX TOROIDAL MAGNETIC SHIELDING

From the derivation of the first part of the equation, it is possible to calculate the MVP for individual regions. It is assumed that the extent of the third orthogonal plane is infinite, but the extent of the third orthogonal plane is finite in the actual MI

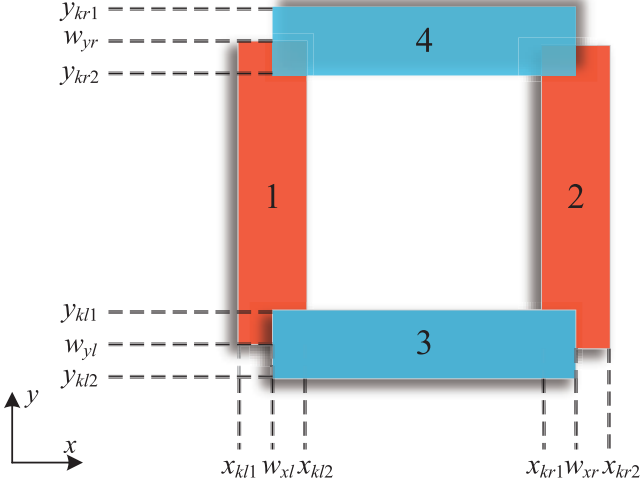


Fig. 6 Simplified model of the coil.

model. Hence, the MVP is made to vary in the third orthogonal plane by the calibration factor. In a coordinate system, the third direction is the three-dimensional space formed perpendicular to the plane comprising the coordinate system and extending outward from that direction. In Fig. 3 the third direction is the y -direction [26].

According to the Biot-Savart law [27], the calibration factor is defined as the ratio of the MFD of an infinite-length linear excitation to the MFD of a finite-length linear excitation.

The rectangular helical coil can be abstracted into four separate conductors, as shown in Fig. 8. The lengths of conductors 1 and 2 in the y -direction are $w_{yr} - w_{yl}$, and the lengths of conductors 3 and 4 in the x -direction are $w_{xr} - w_{xl}$, where the parameter representations can be calculated from (34).

$$\begin{cases} \omega_{xl} = (x_{kl1} + x_{kl2})/2 \\ \omega_{xr} = (x_{kr1} + x_{kr2})/2 \\ \omega_{yl} = (y_{kl1} + y_{kl2})/2 \\ \omega_{yr} = (y_{kr1} + y_{kr2})/2 \end{cases} \quad (34)$$

(35) gives the MFD at a point in an unenclosed region due to two infinitely long parallel conductors, 1 and 2, being excited.

$$B_{1,2}^{\text{inf}} = \left[\left(\frac{k}{h_1} \right)^2 + \left(\frac{k}{h_2} \right)^2 - 2 \left(\frac{k}{h_1 h_2} \right) \cdot \cos(\pi - \gamma_1 - \gamma_2) \right]^{\frac{1}{2}} \quad (35)$$

where the excitation current is I_p , $\Gamma_{xl} = x - w_{xl}$, $\Gamma_{xr} = x - w_{xr}$, $\Gamma_z = z - z_v$, $z_v = z_7 - z_6$, $k = \mu_0 I_p / 2\pi$, the rest of the parameters can be calculated from (36).

$$\begin{cases} \cos \alpha_1 = (x - w_{xl})/g_1 \\ \cos \alpha_2 = (w_{xl} - x)/g_1 \\ h_1 = [(\Gamma_{xl})^2 + (\Gamma_z)^2]^{\frac{1}{2}} \\ h_2 = [(\Gamma_{xr})^2 + (\Gamma_z)^2]^{\frac{1}{2}} \end{cases} \quad (36)$$

(37) gives the MFD in the unconfined area excited by two finite-length conductors, 1 and 2.

$$B_{1,2}^f = \left[(B_1^f)^2 + (B_2^f)^2 - 2B_1^f B_2^f \cdot \cos(\pi - \gamma_1 - \gamma_2) \right]^{\frac{1}{2}} \quad (37)$$

$$B_1^f = \frac{\mu_0 I_p}{4\pi h_1} \cdot \left(\frac{h_4}{\sqrt{h_1^2 + h_4^2}} - \frac{h_3}{\sqrt{h_1^2 + h_3^2}} \right) \quad (38)$$

$$B_2^f = \frac{\mu_0 I_p}{4\pi h_2} \cdot \left(\frac{h_4}{\sqrt{h_2^2 + h_4^2}} - \frac{h_3}{\sqrt{h_2^2 + h_3^2}} \right) \quad (39)$$

where $h_3 = y_{kl1} - y$, $h_4 = y_{kr2} - y$. y_{kl1} and y_{kr2} denote the dimension on the third direction y in the mutual induction model. The flux density excited by a straight line of finite length can be calculated by substituting the derived B_1^f and B_2^f into (37). The calibration factor in the MI model is derived from (40). In the MI model, the calibration factor for the third orthogonal plane can be similarly derived by the above steps.

$$j_{xz}(u, v, w) = \frac{B_{1,2}^f}{B_{1,2}^{\text{inf}}} \quad (40)$$

The literature proposes the coefficient function $g(\mu_i)$ [23], where μ_i denotes the relative permeability of the medium, and $g(\mu_i)$ is a function of μ_i , which reduces the error generated by the relative permeability.

$$g(\mu_i) = \frac{B_z^{3\text{DFEA}}(\mu_i)}{B_z^{2\text{DFEA}}(\mu_i)} \cdot \frac{B_z^{2\text{DFEA}}(\mu_i=1)}{B_z^{3\text{DFEA}}(\mu_i=1)} \quad (41)$$

In the above equation, the z -axis of the MFD derived from the three dimensional and two dimensional FEA models of μ_r at relative permeability are denoted by $B_z^{3\text{DFEA}}(\mu_i)$ and $B_z^{2\text{DFEA}}(\mu_i)$. The MFD in the z -direction derived from three dimensional and two dimensional FEA models of the unconfined region are also denoted by $B_z^{3\text{DFEA}}(\mu_i=1)$ and $B_z^{2\text{DFEA}}(\mu_i=1)$, respectively.

Since the coils are parallel to each other, only the perpendicular z -axis of MFD exists, which plays a role in determining the MI. In this WPT system, the total MFD under the three-dimensional areas is found by summing the subflux densities in each plane and then reducing the error by using calibration factors and coefficient functions $g(\mu_i)$, where the formula is calculated as (42).

$$\begin{cases} B_{zr}^{3\text{D}}(u, v, w) = B_{xz}^{2\text{D}} + B_{yz}^{2\text{D}} \\ B_{xz}^{2\text{D}}(u, v, w) = B_{zr}^{xz}(x, z) \cdot g(\mu_i) \cdot j_{xz}(u, v, w) \\ B_{yz}^{2\text{D}}(u, v, w) = B_{zr}^{yz}(y, z) \cdot g(\mu_i) \cdot j_{xz}(u, v, w) \end{cases} \quad (42)$$

$B_{zr}^{xz}(u, w)$ and $B_{zr}^{yz}(v, w)$ are the z -components of the MFD in the r -region derived from the individual planes in the MI model. Depending on the location of the receiving coil, it is

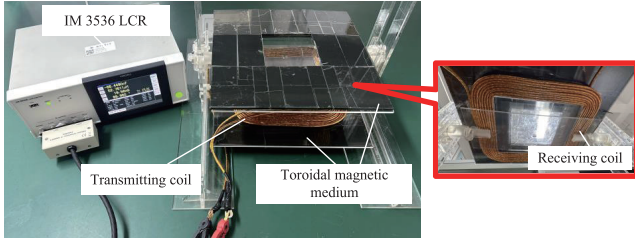


Fig. 7 Experimental equipment.

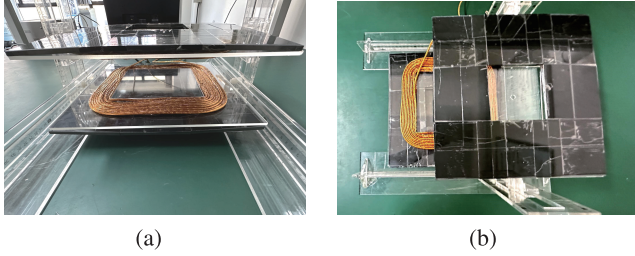


Fig. 8 Relative position change of experimental model coils. (a) Vertical offset. (b) Horizontal offset.

therefore necessary to find $B_{zr}^{3D}(u, v, w)$ to further calculate the MI of this WPT system. The MI is given by (43).

$$M = \sum_{e_r=1}^{E_r} \left(\oint_{S_{er}} B_{zr}^{3D}(u, v, w) dx dy \right) / I_p \quad (43)$$

where E_r denotes the winding count of the receiving coil, e_r denotes coil per turn, and S_{er} denotes the effective receiving area per winding count of the coil.

IV. VERIFICATION

Accuracy for (43) is verified through simulations conducted using ANSYS Maxwell software. As shown in Fig. 7, impedance tester, acrylic frame and other devices is used for the measurements. The experiments are conducted on a non-magnetic wooden table with an acrylic frame, and an impedance tester is used for testing. The transmitting and receiving side magnetic shields are constructed of 5 mm high permeability cabochon ring type magnetic shields placed outside the transceiver coils, respectively. The copper wire coil has a radius of 4 mm and contains ten turns. Current frequency set to 85 KHz. Coil and dielectric material parameters and coil harmonic parameters are illustrated in Table I and Table II.

This section will examine the offset variation of the coil in the horizontal and vertical directions. During the experiment, the transmitting side device was kept fixed and the receiving side device was adjusted for vertical and horizontal relative offset positions. The variation of the relative places of the coils in the experimental model is illustrated in Fig. 8.

A. Vertical Offset

For the receiving coil vertical offset experiment, set the initial distance between the receiving and transmitting coils to 30

TABLE I
COIL AND DIELECTRIC MATERIAL PARAMETERS

Symbol	Parameter	Value
N_p	Transmitting coil winding count	10
N_s	Receiving coil winding count	10
L_c	Copper wire diameter	4 mm
L_g	Gap between coil and magnetic shield	5 mm
μ_r	Relative permeability of ferrite	2800
I_p	Transmitting coil excitation current	10 A
f	Current frequency	85 kHz
H_e	Height of inner edge	5 mm
L_x	Coil size in x -direction	256 mm
L_y	Coil size in y -direction	261 mm

TABLE II
COIL HARMONIC PARAMETERS

Harmonic number	Value
Harmonic ($N_{2a}, N_{2b}, N_{2c}, N_{2d}, N_{2e}, N_{4a}, N_{4b}, N_{4c}, N_{4d}, N_{4e}, N_{8a}, N_{8b}, N_{8c}, N_{8d}, N_{8e}, N_{10a}, N_{10b}, N_{10c}, N_{10d}, N_{10e}$)	40
Harmonic ($N_1, N_3, N_5, N_9, N_{11}, N_{6a}, N_{6b}, N_{6c}, N_{6d}, N_{6e}, L_{6a}, L_{6b}, L_{6c}, L_{6d}, L_{6e}, N_7$)	100
Harmonic ($L_{2a}, L_{2b}, L_{2c}, L_{2d}, L_{2e}, L_{4a}, L_{4b}, L_{4c}, L_{4d}, L_{4e}, L_{8a}, L_{8b}, L_{8c}, L_{8d}, L_{8e}, L_{10a}, L_{10b}, L_{10c}, L_{10d}, L_{10e}$)	40

mm, and the receiving side unit is gradually moved to 120 mm in 10 mm increments along the z -direction. The offset schematic is depicted in Fig. 9.

In Fig. 9, Δz denotes the dynamic spacing between coils. The green dashed line signifies the location of the receiving coil before the vertical offset, the blue solid line signifies the position of the receiving coil after the vertical offset, and the red solid line indicates the place of the transmitting coil. The MI data and error comparisons after the vertical offset of the receiving coil are recorded in Table III. Where M_c represents computational MI, M_s represents simulated MI, and M_e represents experimental MI. ε_1 denotes the mistake between the MI of the M_c and M_s , ε_2 denotes the bias between the MI of the M_c and M_e . Such expressions will be adhered to in the following parts of this article. The expressions for ε_1 and ε_2 are given by (44) and (45), respectively.

$$\varepsilon_1 = \frac{|M_c - M_s|}{M_c} \times 100\% \quad (44)$$

$$\varepsilon_2 = \frac{|M_c - M_e|}{M_c} \times 100\% \quad (45)$$

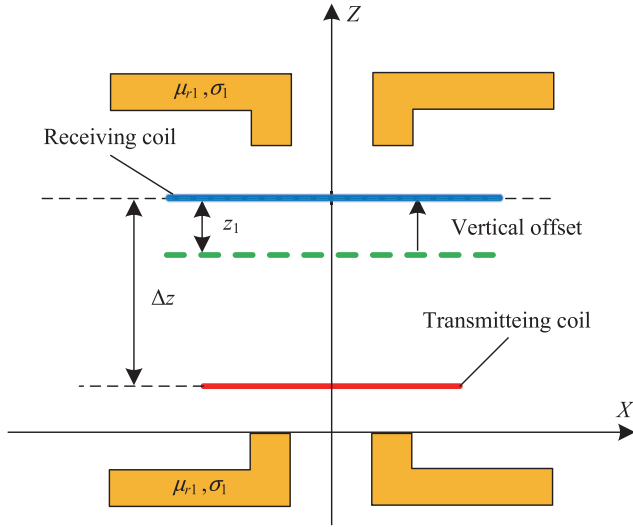


Fig. 9 Schematic diagram of the vertical offset of the receiving coil.

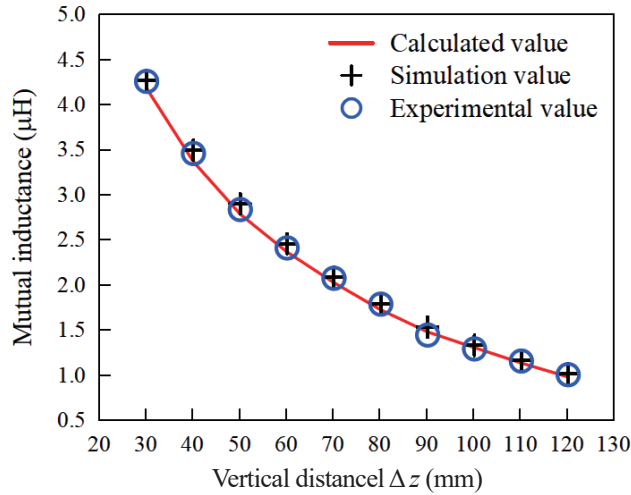


Fig. 10 MI variation curve with vertical distance of receiving coil.

Analysis of the data in Table III reveals that the error ε_1 between the M_c and M_s remains below 4.55%, and the error ε_2 between the M_c and M_e does not exceed 4.69% for Δz ranging from 30 mm-120 mm. The error between the M_c , M_s and M_e values of mutual inductance is within 5% and the experimental results are in better agreement. Based on Table III, a plot of MI versus vertical distance between coils was illustrated as exhibited in Fig. 10.

The curve in Fig. 10 shows that MI decreases gradually with increasing Δz . This is due to the fact that the increase in Δz causes a gradual decrease in MFD in the MI model and hence the MI value of this system gradually decreases.

B. Horizontal Offset

For the receiving coil horizontal offset experiment, Δz in the MI model is maintained at a constant 40 mm. In the experiment, the receiving coil is positioned in the horizontal directions in increments of 10 mm, beginning from the horizontal

TABLE III
MUTUAL INDUCTANCE AND DEVIATION AT VERTICAL OFFSET

Δz (mm)	M_c (μH)	M_s (μH)	M_e (μH)	ε_1	ε_2
30	4.0896	4.2756	4.2667	4.55%	4.33%
40	3.3774	3.504	3.2189	3.75%	4.69%
50	2.7956	2.9119	2.7281	4.16%	2.41%
60	2.3771	2.4677	2.4234	3.81%	1.95%
70	2.0385	2.0965	2.0876	2.85%	2.41%
80	1.7372	1.7985	1.8011	3.53%	3.68%
90	1.4926	1.5451	1.4591	3.52%	2.24%
100	1.3194	1.3424	1.3053	1.74%	1.07%
110	1.1485	1.1802	1.1712	2.76%	1.98%
120	0.9943	1.0314	1.0194	3.73%	2.52%

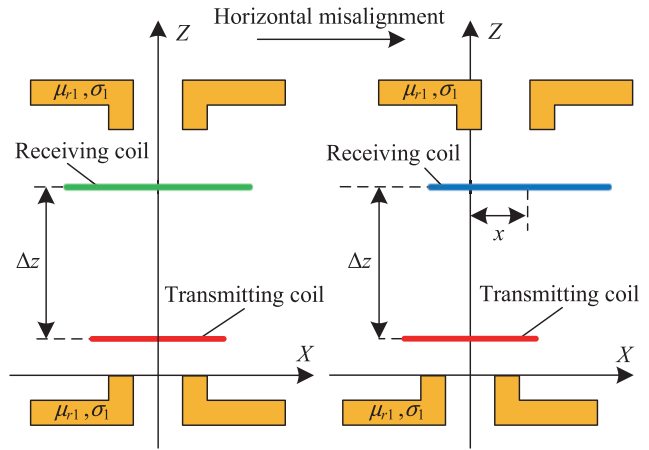


Fig. 11 Schematic diagram of the horizontal offset of the receiving coil.

coordinate $x = 0$ mm and extending to $x = 50$ mm and $x = -50$ mm, respectively. The offset schematic is depicted in Fig. 11. The MI measurements and their error comparisons when the receiving coil is horizontally offset are recorded in Table IV. In the table, x denotes the horizontal offset of the receiving coil, and this notation will be used in the subsequent sections.

Analysis of the findings in Table IV indicates that when the horizontal offset range $x = -20$ mm, the error between the M_c and M_s values does not exceed 4.0% in all cases except for the MI where the deviation ε_1 between the M_c and M_s is 4.41%. The error ε_2 between the M_c and M_e of MI does not exceed a maximum of 4.31% and reaches a minimum of 1.77%. This indicates a high level of agreement among the results of calculated MI, simulated MI, and experimental MI. According to Table IV, the modification of MI with horizontal offset distance between the coils is graphed as exhibited in Fig. 12.

Fig. 12 exhibits that when the vertical height is maintained constant, the receiving coil is moved in horizontal direction. MI decreases as the distance from the center position increases. This is due to the fact that in this system the magnetic flux

TABLE IV
HORIZONTAL OFFSET MUTUAL INDUCTANCE AND ERROR
AT VERTICAL DISTANCE $\Delta z=40$ MM

$x(\text{mm})$	$M_c(\mu\text{H})$	$M_s(\mu\text{H})$	$M_e(\mu\text{H})$	ϵ_1	ϵ_2
-50	2.6969	2.7442	2.5936	1.75%	3.83%
-40	2.8982	2.9817	2.8163	2.88%	2.83%
-30	3.0775	3.1801	2.9628	3.33%	3.73%
-20	3.1967	3.3376	3.0590	4.41%	4.31%
-10	3.3036	3.4344	3.2349	3.96%	2.08%
0	3.4097	3.5029	3.2773	2.73%	3.88%
10	3.3253	3.4241	3.2427	2.97%	2.48%
20	3.2013	3.3218	3.1446	3.76%	1.77%
30	3.0781	3.1664	2.9458	2.87%	4.30%
40	2.8909	2.9732	2.8125	2.85%	2.71%
50	2.6876	2.7391	2.5774	1.92%	4.10%

TABLE V
COMPARISON OF TIME TAKEN FOR COMPUTATION AND
SIMULATION OF MUTUAL INDUCTANCE

$t_c(\text{s})$	$T_a(\text{s})$	$T_b(\text{s})$	$T_c(\text{s})$
t_1	82.56	95.66	79.37
t_2	86.46	94.24	81.34
t_3	84.56	92.69	81.09
t_4	82.56	97.66	80.45
t_5	81.67	91.23	77.13
t_6	8.41	8.89	6.90
t_7	7.23	8.79	7.32
t_8	8.65	8.63	6.90
t_9	7.89	9.69	8.30
t_{10}	8.79	8.32	8.12

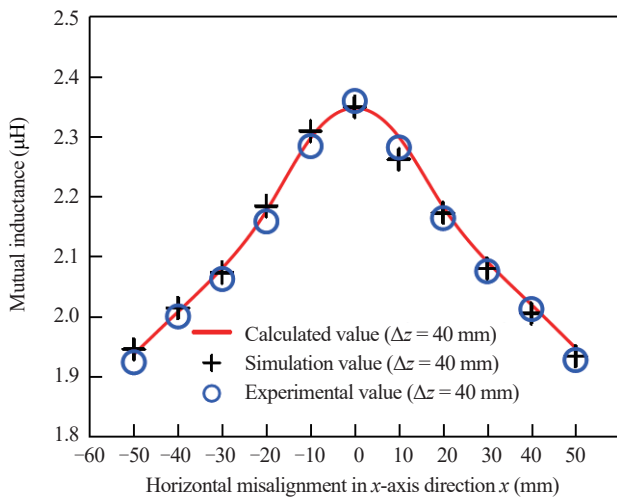


Fig. 12 MI variation curve with horizontal offset of receiving coil.

decreases gradually from the center to the edges and hence the value of MI decreases gradually as x increases.

C. Comparison

The speed of the computational model presented in the article is compared with the simulation software ANSYS Maxwell for solving MI under the same conditions using the computational software MATLAB. Ignoring the time spent on ANSYS Maxwell modeling, the MI model of a bounded magnetically shielded rectangular coil with a convex toroidal type has been computed in MATLAB and simulated in ANSYS Maxwell using the same hardware configuration. The results of the comparison of the solution speeds of the two methods are presented in Table V. In the table, t_c represents the time taken for testing, t_{1-5} indicates the average time taken for ANSYS Maxwell simulation, and t_{6-10} indicates the average time taken for MATLAB computation. T_a indicates the duration for the computation or

simulation of the MI value at vertical offset. T_b indicates the duration for the computation or simulation of the MI value at the horizontal offset. T_c indicates the duration for the computation or simulation of the MI values at horizontal and vertical offsets. The data analysis in Table V reveals that the fastest time for ANSYS Maxwell simulation is 77.13 seconds. In contrast, the longest time taken by the MATLAB programme employing the methodology of this article was 9.79 seconds, which is considerably shorter than the simulation time of ANSYS Maxwell. This demonstrates the significant computational efficiency advantage of the method used in this article.

The parameters from Tables I and II are incorporated into the system, and the ANSYS Maxwell model output depicting the z - x magnetic field distribution cross-section for the coaxial state with $\Delta z = 40$ mm and the horizontal offset state with $x = -50$ mm is presented in Fig. 13.

Fig. 13 represents a graphical representation of the spatial distribution of MVP in this system at $\Delta z = 40$ mm. The coaxial state and the horizontal offset state magnetic field distribution comparison graph indicate that MFD shows a gradual increase in the horizontal direction, followed by a gradual decrease, consistent with the distributional properties of MFD in this structure.

For the comparison of the calculation methodology used in the cited literature with the methodology presented in this article, the outcome are shown in Table VI, where VO represents vertical offsets, HO represents horizontal offsets, MS represents with magnetic shielding, FMS represents with bounded magnetic shielding, and SM represents the ability to save consumables.

The convex ring type magnetic shielding material presented in the article is replaced with the rectangular disc magnetic shielding material of the exact specifications, according to the parameters in Tables I and II. This article compares it to the transmission structure. The findings indicate that the material consumption is lowered by 11.12% with the convex ring type magnetic shielding material, compared to the rectangular disc

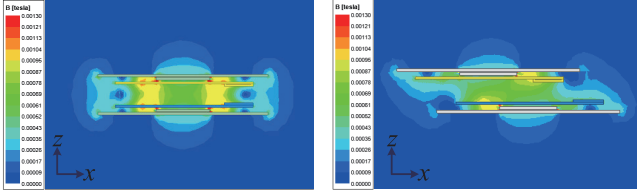


Fig. 13 Comparative analysis of magnetic field morphology.

TABLE VI
COMPARISON OF CALCULATION METHODS

	VO	HO	MS	FMS	SM
[19]	√	×	×	×	×
[20]	√	√	×	×	×
[23]	×	√	√	×	×
[24]	√	√	√	×	×
[26]	×	×	√	√	×
[27]	√	√	√	√	×
This paper	√	√	√	√	√

magnetic shielding material. Furthermore, the percentage of material savings for this model increases even more as the area of the transmission structure skeletonized with the toroidal magnetic shielding material increases.

Additionally, the investigation is conducted to examine the difference in the impact of magnetic shielding material on MI between a convex ring type and a rectangular disc using the same coil structure. With Table I and Table II, two kinds of power transmission models are constructed. The MI ratio is compared through simulation analysis when the magnetic medium is a convex ring type versus a rectangular disc. In this comparison, the rectangular disc magnetic shielding area is identical to the cabochon ring type, 300 mm×300 mm. The other coils and related parameters remain unchanged from those of the cabochon ring-type magnetic shielding transmission structure.

Within conventional mutual-inductance models, for instance those utilizing a rectangular plate magnetic shielding transmission system, that system performance stays relatively stable. Should the performance of the MI model presented in this study surpass 97% of that of the original model, it can be inferred that this WPT system has effectively met the objectives of diminishing production expenses while concurrently preserving transmission performance. Therefore, the simulated MI ratio data for the two transmission structures in the case of vertical offset and horizontal offset are provided in this article, as shown in Tables VII and VIII. In these tables, Δz represents the vertical offset distance, and x denotes the horizontal offset distance. ε_3 denotes the ratio of MI values between the convex annular magnetic medium and the rectangular disc magnetic medium in the WPT system. M_u and M_v respectively indicate the MI for the convex ring and rectangular disc magnetically shielded structures. The expression for ε_3 is presented in (46).

TABLE VII
COMPARISON WITH RECTANGULAR DISC MAGNETICALLY SHIELDED TRANSMISSION STRUCTURE IN VERTICAL OFFSET SIMULATION OF MUTUAL INDUCTANCE

Δz (mm)	M_u (μH)	M_v (μH)	ε_3
30	4.2756	4.2667	99.79%
40	3.5040	3.4989	99.85%
50	2.9119	2.9081	99.87%
60	2.4677	2.4434	99.02%
70	2.0965	2.0876	99.58%
80	1.7985	1.7911	99.59%
90	1.5451	1.5191	98.32%
100	1.3424	1.3193	98.28%
110	1.1802	1.1712	99.24%
120	1.0314	1.0194	98.84%

TABLE VIII
COMPARISON OF MAGNETIC SHIELDED TRANSMISSION STRUCTURES WITH RECTANGULAR DISCS IN HORIZONTAL OFFSET SIMULATION OF MUTUAL INDUCTANCE

x (mm)	M_u (μH)	M_v (μH)	ε_3
-50	2.7442	2.6969	98.28%
-40	2.9817	2.8982	97.20%
-30	3.1801	3.0775	96.77%
-20	3.3376	3.2967	98.77%
-10	3.4344	3.3536	97.65%
0	3.5029	3.4097	97.34%
10	3.4241	3.3253	97.11%
20	3.3218	3.2713	98.48%
30	3.1664	3.0781	97.21%
40	2.9732	2.8909	97.23%
50	2.7391	2.6876	98.12%

$$\varepsilon_3 = \frac{M_v}{M_u} \times 100\% \quad (46)$$

In summary, whether a vertical offset or a horizontal offset, the simulated ratio of MI between the convex ring-type magnetic shielding transmission structure and the rectangular disc magnetic shielding transmission structure remains above 97.11%. Additionally, ε_3 achieve a maximum of 99.87%. This indicates that this WPT system has largely maintained the transmission performance of the original MI model. Hence, material savings are achieved with convex ring-type magnetically shielded power transmission structures while maintaining transmission efficiencies nearly identical to those of rectangular disc magnetically shielded structures. The manufacturing cost of this WPT system has also been effectively lowered.

V. CONCLUSION

This article presents a model for MI calculation of a rectangular coil with a convex toroidal bounded magnetic shield, proposing an analytical method leveraging spatial boundary separation for precise calculations in complex regions. The method solves the MI calculation formulas in each region through the double Fourier transform, Maxwell's system of equations, and the Biot-Savart law. The calculated results are verified for validity through simulation and experiment, with the findings indicating that the maximum error between them is 4.55%. The MI calculated, simulated, and experimental values are in agreement. The model achieves an 11.12% material saving over the conventional rectangular magnetic shielding transmission structure, with savings increasing with the open-work area of the ring magnetic shielding.

Simultaneously, the MI value of this WPT system can achieve 99.87% of conventional WPT systems. The design can maximize material savings in the structure while ensuring transmission efficiency, possessing more pronounced practical functionality and widespread applicability. In addition, the proposed coil structure model and the results of the study provide theoretical support for the optimisation of the structure and variable of WPT systems, while also instituting a practical basis for the further advancement of MI calculation methods for WPT systems and the widespread application of more reliable and affordable wireless power transfer equipment.

In the end, this study provides a valuable reference and guideline for subsequent research on MI calculations for solenoid-type

magnetically shielded rectangular coil structures.

APPENDIX A

In the matrix transformation process, (30) can be further derived as (33). $[D]$ indicates the unknown in MVP, which contains the the elements of the unknown coefficients. $[K]$ indicates denotes the coefficients of the unknowns, which contains the elements of the known coefficients. $[O]$ and the matrix is populated with elements representing the current sources in the equation. (47) and (48) give the extended forms of $[D]$ and $[O]$, respectively.

$$[D] = \begin{bmatrix} [D_1] & [D_{2a}] & [D_{2b}] & [D_{2c}] & [D_{2d}] & [D_{2e}] & [D_3] & [D_{4a}] & [D_{4b}] \\ [D_{4c}] & [D_{4d}] & [D_{4e}] & [D_5] & [D_{6a}] & [D_{6b}] & [D_{6c}] & [D_{6d}] & [D_{6e}] & [D_7] \\ [D_{8a}] & [D_{8b}] & [D_{8c}] & [D_{8d}] & [D_{8e}] & [D_9] & [D_{10a}] & [D_{10b}] & [D_{10c}] \\ [D_{10d}] & [D_{10e}] & [D_{11}] & & & & & & & \end{bmatrix}^T \quad (47)$$

Each element of $[D]$ consists of a submatrix, the elements of which represent the unknown coefficients of vector magnetic potential.

$$[O] = \begin{bmatrix} [O_1] & [O_{2a}] & [O_{2b}] & [O_{2c}] & [O_{2d}] & [O_{2e}] & [O_3] & [O_{4a}] & [O_{4b}] \\ [O_{4c}] & [O_{4d}] & [O_{4e}] & [O_5] & [O_{6a}] & [O_{6b}] & [O_{6c}] & [O_{6d}] & [O_{6e}] & [O_7] \\ [O_{8a}] & [O_{8b}] & [O_{8c}] & [O_{8d}] & [O_{8e}] & [O_9] & [O_{10a}] & [O_{10b}] & [O_{10c}] \\ [O_{10d}] & [O_{10e}] & [O_{11}] & & & & & & & \end{bmatrix}^T \quad (48)$$

where each element of the $[O]$ is a submatrix, the elements represent the current sources contained within the vector magnetic potentials. $[K]$ and its elements are provided by (49).

$$[K] = \begin{bmatrix} [V_1] & [V_0] \\ [V_0] & [V_{2a\&2e}] & [V_0] \\ [V_0] & [V_0] & [V_3] & [V_0] \\ [V_0] & [V_0] & [V_0] & [V_{4a\&4e}] & [V_0] \\ [V_0] & [V_0] & [V_0] & [V_0] & [V_5] & [V_0] & [V_0] & [V_0] & [V_0] & [V_0] & [V_0] \\ [V_0] & [V_0] & [V_0] & [V_0] & [V_0] & [V_{6a\&6e}] & [V_0] & [V_0] & [V_0] & [V_0] & [V_0] \\ [V_0] & [V_0] & [V_0] & [V_0] & [V_0] & [V_0] & [V_7] & [V_0] & [V_0] & [V_0] & [V_0] \\ [V_0] & [V_{8a\&8e}] & [V_0] & [V_0] & [V_0] \\ [V_0] & [V_9] & [V_0] & [V_0] \\ [V_0] & [V_{10a\&10e}] & [V_0] \\ [V_0] & [V_{11}] \end{bmatrix} \quad (49)$$

where $[V]$ is a submatrix within $[K]$. Each element of matrix $[V]$ is also a submatrix, where $[V_0]$ represents the zero matrix, and the elements of other submatrices represent known coefficients of the vector magnetic potential. The submatrices of $[V]$ are specifically represented from (50) to (60).

$$[V_1] = [[I] [C_1^{2a}] [C_1^{2b}] [C_1^{2c}] [C_1^{2d}] [C_1^{2e}]] \quad (50)$$

$$[V_3] = [[C_3^{2a}] [C_3^{2b}] [C_3^{2c}] [C_3^{2d}] [C_3^{2e}] \\ [I] [C_3^{4a}] [C_3^{4b}] [C_3^{4c}] [C_3^{4d}] [C_3^{4e}]] \quad (51)$$

$$[V_5] = [[C_5^{4a}] [C_5^{4b}] [C_5^{4c}] [C_5^{4d}] [C_5^{4e}] \\ [I] [C_5^{6a}] [C_5^{6b}] [C_5^{6c}] [C_5^{6d}] [C_5^{6e}]] \quad (52)$$

$$[V_7] = [[C_7^{6a}] [C_7^{6b}] [C_7^{6c}] [C_7^{6d}] [C_7^{6e}] \\ [I] [C_7^{8a}] [C_7^{8b}] [C_7^{8c}] [C_7^{8d}] [C_7^{8e}]] \quad (53)$$

$$[V_9] = [[C_9^{8a}] [C_9^{8b}] [C_9^{8c}] [C_9^{8d}] [C_9^{8e}] \\ [I] [C_9^{10a}] [C_9^{10b}] [C_9^{10c}] [C_9^{10d}] [C_9^{10e}]] \quad (54)$$

$$[V_{11}] = [[C_{11}^{10a}] [C_{11}^{10b}] [C_{11}^{10c}] [C_{11}^{10d}] [C_{11}^{10e}] [I]] \quad (55)$$

$$[V_{2a\&2e}] = \begin{bmatrix} [C_{2a}^1] & [I] & [C_{2a}^{2b}] & [0] & [0] & [0] & [C_{2a}^3] \\ [C_{2b}^1] & [C_{2b}^{2a}] & [I] & [C_{2b}^{2c}] & [0] & [0] & [C_{2b}^3] \\ [C_{2c}^1] & [0] & [C_{2c}^{2b}] & [I] & [C_{2c}^{2d}] & [0] & [C_{2c}^3] \\ [C_{2d}^1] & [0] & [0] & [C_{2d}^{2c}] & [I] & [C_{2d}^{2e}] & [C_{2d}^3] \\ [C_{2e}^1] & [0] & [0] & [0] & [C_{2e}^{2d}] & [I] & [C_{2e}^3] \end{bmatrix} \quad (56)$$

$$[V_{4a\&4e}] = \begin{bmatrix} [C_{4a}^3] & [I] & [C_{4a}^{4b}] & [0] & [0] & [0] & [C_{4a}^5] \\ [C_{4b}^3] & [C_{4b}^{4a}] & [I] & [C_{4b}^{4c}] & [0] & [0] & [C_{4b}^5] \\ [C_{4c}^3] & [0] & [C_{4c}^{4b}] & [I] & [C_{4c}^{4d}] & [0] & [C_{4c}^5] \\ [C_{4d}^3] & [0] & [0] & [C_{4d}^{4c}] & [I] & [C_{4d}^{4e}] & [C_{4d}^5] \\ [C_{4e}^3] & [0] & [0] & [0] & [C_{4e}^{4d}] & [I] & [C_{4e}^5] \end{bmatrix} \quad (57)$$

$$[V_{6a\&6e}] = \begin{bmatrix} [C_{6a}^5] & [I] & [C_{6a}^{6b}] & [0] & [0] & [0] & [C_{6a}^7] \\ [C_{6b}^5] & [C_{6b}^{6a}] & [I] & [C_{6b}^{6c}] & [0] & [0] & [C_{6b}^7] \\ [C_{6c}^5] & [0] & [C_{6c}^{6b}] & [I] & [C_{6c}^{6d}] & [0] & [C_{6c}^7] \\ [C_{6d}^5] & [0] & [0] & [C_{6d}^{6c}] & [I] & [C_{6d}^{6e}] & [C_{6d}^7] \\ [C_{6e}^5] & [0] & [0] & [0] & [C_{6e}^{6d}] & [I] & [C_{6e}^7] \end{bmatrix} \quad (58)$$

$$[V_{8a\&8e}] = \begin{bmatrix} [C_{8a}^7] & [I] & [C_{8a}^{8b}] & [0] & [0] & [0] & [C_{8a}^9] \\ [C_{8b}^7] & [C_{8b}^{8a}] & [I] & [C_{8b}^{8c}] & [0] & [0] & [C_{8b}^9] \\ [C_{8c}^7] & [0] & [C_{8c}^{8b}] & [I] & [C_{8c}^{8d}] & [0] & [C_{8c}^9] \\ [C_{8d}^7] & [0] & [0] & [C_{8d}^{8c}] & [I] & [C_{8d}^{8e}] & [C_{8d}^9] \\ [C_{8e}^7] & [0] & [0] & [0] & [C_{8e}^{8d}] & [I] & [C_{8e}^9] \end{bmatrix} \quad (59)$$

$$[V_{10a\&10e}] = \begin{bmatrix} [C_{10a}^9] & [I] & [C_{10a}^{10b}] & [0] & [0] & [0] & [C_{10a}^{11}] \\ [C_{10b}^9] & [C_{10b}^{10a}] & [I] & [C_{10b}^{10c}] & [0] & [0] & [C_{10b}^{11}] \\ [C_{10c}^9] & [0] & [C_{10c}^{10b}] & [I] & [C_{10c}^{10d}] & [0] & [C_{10c}^{11}] \\ [C_{10d}^9] & [0] & [0] & [C_{10d}^{10c}] & [I] & [C_{10d}^{10e}] & [C_{10d}^{11}] \\ [C_{10e}^9] & [0] & [0] & [0] & [C_{10e}^{10d}] & [I] & [C_{10e}^{11}] \end{bmatrix} \quad (60)$$

where $[I]$ signifies the unit matrix. The submatrix $[C]$ signifies the coefficients of the array of equations. And a linear equation represents each row of the matrix.

REFERENCES

- [1] Y. Wang and C. C. Mi, "Guest editorial: special issue on advanced and emerging technologies of high efficiency and long-distance wireless power transfer systems," in *IEEE Transactions on Industry Applications*, vol. 58, no. 1, pp. 1006–1009, Jan.-Feb. 2022.
- [2] S. Y. R. Hui, "Past, present and future trends of non-radiative wireless power transfer," in *CPSS Transactions on Power Electronics and Applications*, vol. 1, no. 1, pp. 83–91, Dec. 2016.
- [3] S. Y. Chu, X. Cui, X. Zan, and A. -T. Avestruz, "Transfer-power measurement using a non-contact method for fair and accurate metering of wireless power transfer in electric vehicles," in *IEEE Transactions on Power Electronics*, vol. 37, no. 2, pp. 1244–1271, Feb. 2022.
- [4] M. Liang, K. E. K. Drissi, and C. Pasquier, "Frequency domain analysis of a dynamic wireless transfer system for electric vehicles," in *IEEE Access*, vol. 12, pp. 72777–72793, 2024.
- [5] P. K. Chittoor and C. Bharatiraja, "Wireless-sensor communication based wireless-charging coil positioning system for UAVs with maximum power point tracking," in *IEEE Sensors Journal*, vol. 22, no. 8, pp. 8175–8182, Apr. 2022.
- [6] D. Kim and S. Lee, "Propulsion and control of microrobot using a multi-selective wireless power transfer coil," in *IEEE Transactions on Magnetics*, vol. 59, no. 11, pp. 1–6, Nov. 2023.
- [7] Q. Wang, W. Che, M. Mongiardo, and G. Monti, "Wireless power transfer system with high misalignment tolerance for bio-medical implants," in *IEEE Transactions on Circuits and Systems II: Express Briefs*, vol. 67, no. 12, pp. 3023–3027, Dec. 2020.
- [8] T. Campi, S. Cruciani, F. Maradei, A. Montalto, F. Musumeci, and M. Feliziani, "Centralized high power supply system for implanted medical devices using wireless power transfer technology," in *IEEE Transactions on Medical Robotics and Bionics*, vol. 3, no. 4, pp. 992–1001, Nov. 2021.
- [9] A. Wibisono, M. H. Alsharif, H. -K. Song, and B. M. Lee, "A survey on underwater wireless power and data transfer system," in *IEEE Access*, vol. 12, pp. 34942–34957, 2024.
- [10] Z. Yan, B. Song, Y. Zhang, K. Zhang, Z. Mao, and Y. Hu, "A rotation-free wireless power transfer system with stable output power and efficiency for autonomous underwater vehicles," in *IEEE Transactions on Power Electronics*, vol. 34, no. 5, pp. 4005–4008, May 2019.
- [11] D. Wu, C. Huang, F. Yang, and Q. Sun, "Analytical calculations of self- and mutual inductance for rectangular coils with lateral misalignment in inductive power transfer," in *IET Power Electronics*, vol. 12, no. 15, Oct.

- 2019.
- [12] R. Oliveira and P. Lehn, "An improved mutual inductance electromagnetic model for inductive power transfer systems under misalignment conditions," in *IEEE Transactions on Vehicular Technology*, vol. 69, no. 6, pp. 6079–6093, Jun. 2020.
- [13] J. T. Conway, "Inductance calculations for circular coils of rectangular cross section and parallel axes using bessel and struve functions," in *IEEE Transactions on Magnetics*, vol. 46, no. 1, pp. 75–81, Jan. 2010.
- [14] S. Babic, F. Sirois, C. Akyel, G. Lemarquand, V. Lemarquand, and R. Ravaut, "New formulas for mutual inductance and axial magnetic force between a thin wall solenoid and a thick circular coil of rectangular cross-section," in *IEEE Transactions on Magnetics*, vol. 47, no. 8, pp. 2034–2044, Aug. 2011.
- [15] I. Jeong and K. Nam, "Analytic expressions of torque and inductances via polynomial approximations of flux linkages," in *IEEE Transactions on Magnetics*, vol. 51, no. 7, pp. 1–9, Jul. 2015.
- [16] Y. Cheng and Y. Shu, "A new analytical calculation of the mutual inductance of the coaxial spiral rectangular coils," in *IEEE Transactions on Magnetics*, vol. 50, no. 4, pp. 1–6, Apr. 2014.
- [17] D. Wu, Q. Sun, X. Wang, and F. Yang, "Analytical model of mutual coupling between rectangular spiral coils with lateral misalignment for wireless power applications," in *IET Power Electronics*, vol. 11, no. 5, pp. 781–786, May 2018.
- [18] D. Wu, F. Cheng, and C. Huang, "Analytical computation of mutual inductance between two rectangular spiral coils with misalignments for wireless power applications," in *Microwave and Optical Technology Letters*, vol. 62, Oct. 2019.
- [19] Y. Cheng and Y. Shu, "Mutual inductance calculation between arbitrarily positioned rectangular filaments," in *International Journal of Applied Electromagnetics and Mechanics*, vol. 46, no. 1, pp. 287–298, Feb. 2014.
- [20] Z. Luo and X. Wei, "Analysis of square and circular planar spiral coils in wireless power transfer system for electric vehicles," in *IEEE Transactions on Industrial Electronics*, vol. 65, no. 1, pp. 331–341, Jan. 2018.
- [21] Z. Li, J. Li, C. Quan, X. Zhang, and S. Huang, "Mutual inductance calculation of arbitrarily positioned rectangular coils with magnetic shielding in wireless power transfer systems," in *Transactions of China Electrotechnical Society*, vol. 37, no. 17, pp. 4294–4305, Sept. 2022.
- [22] B. K. Kushwaha, G. Rituraj, and P. Kumar, "3-d analytical model for computation of mutual inductance for different misalignments with shielding in wireless power transfer system," in *IEEE Transactions on Transportation Electrification*, vol. 3, no. 2, pp. 332–342, Jun. 2017.
- [23] B. K. Kushwaha, G. Rituraj, and P. Kumar, "A subdomain analytical model of coil system with magnetic shields of finite dimensions and finite permeability for wireless power transfer systems," in *IEEE Transactions on Magnetics*, vol. 56, no. 12, pp. 1–11, Dec. 2020.
- [24] Z. Chen, Z. Li, Z. Lin, J. Li, and Y. Zhang, "Mutual inductance calculation of rectangular coils at arbitrary position with bilateral finite magnetic shields in wireless power transfer systems," in *IEEE Transactions on Power Electronics*, vol. 39, no. 10, pp. 14065–14076, Oct. 2024.
- [25] H. Li, C. Wang, Z. Wei, and D. Li, "Research of shield structure for wireless power transfer system," in *Advanced Technology of Electrical Engineering and Energy*, vol. 38, no. 05, pp. 74–83, May 2019.
- [26] A. Demenko, R. M. Wojciechowski, and J. K. Sykulski, "2-d versus 3-d electromagnetic field modeling in electromechanical energy converters," in *IEEE Transactions on Magnetics*, vol. 50, no. 2, pp. 897–900, Feb. 2014.
- [27] Z. Zhang, M. Shao, K. Shang, X. Li, C. Huang, J. Shi, H. Cui, and Y. Dong, "Mutual inductance calculation between arbitrarily positioned polygonal coils," in *Transactions of Nanjing University of Aeronautics & Astronautics*, vol. 39, no. S1, pp. 120–126, Oct. 2022.



soft-switching power converters.

Zhongqi Li was born in China in 1985. He received the M.Sc. degree from Hunan University of Technology in 2012, and the Ph.D. degree from the Hunan University in 2016. From 2016, he is working assistant professor in Hunan University of Technology. From 2020, he is now working post-doctoral fellow in Hunan University. His research interests include wireless power transfer systems and



Qian Zhang was born in China in 1999. He received a bachelor's degree in software engineering from Wuhan Polytechnic University in 2023. He is currently pursuing the Master's degree in Control Science and Engineering at Hunan University of Technology. His current research interests include wireless power transfer systems.



Lingjun Kong was born in China in 1998. He received a bachelor's degree in Electrical Engineering and Automation from Xuchang University, Xuchang, China, in 2020. He is currently pursuing the Master's degree in Energy Power at Hunan University of Technology. His current research interests include wireless power transfer systems.



Changxuan Hu was born in China in 1999. He received a bachelor's degree from School of Electrical Engineering, Henan Polytechnic University in 2021. He is pursuing a Master's degree in the School of Rail Transportation at Hunan University of Technology, majoring in wireless power transfer technology.



Shoudao Huang received the B.Eng. and Ph.D. degrees in electrical engineering from the College of Electrical and Information Engineering, Hunan University, Changsha, China, in 1983, and 2005, respectively. He is currently a Full-Time Professor with the College of Electrical and Information Engineering, Hunan University. His research interests include motor design and control, power electronic system and control, and wind energy conversion systems.